Introduction

1.1 Background

In the last few decades, significant researches has been dedicated to magnetic nanoparticles (MNP_S) with desirable properties for specific applications such as electronic (e.g. magnetic data storage, sensors, xerography) and clinical industries (e.g. magnetic hyperthermia treatment, MHT, magnetic resonance imaging, MRI, drug delivery, theranostics, immunoassays, cells separation, manipulation of biochemical products and tissues recovery) [1-10]. Moreover, these MNP_S are also explored for waste treatment and battery applications [11, 12]. The present thesis focuses on the synthesis and characterization of pure and substituted iron carbides. It also describes the suitability of these MNPs for MHT, photocatalysis, and as anode materials for Li-ion batteries (LIB_S). A brief discussion about the applications, properties, and synthesis protocols for iron carbides are given below:

1.2 Magnetic hyperthermia

There are numerous techniques for cancer treatments which can be listed as radiation therapy, chemotherapy, immunotherapy, targeted therapy, hormone therapy, stem cell transplant, precision medicine, hyperthermia, magnetic hyperthermia (MHT) etc. [13-20]. In medical oncology, the term hyperthermia refers to a therapeutic method

by which a localized region is subjected to an external source of heat to raise the temperature between 42-46 °C to kill the cancerous cells or inhibit their abnormal growth [21-35]. However, at the higher temperature (>50 °C), it is termed as thermal ablation. Out of various hyperthermia treatments, MHT is suggested to have uniform temperature distribution near the affected area and cause lower side effects [5, 36, 37]. It is because of nanometric size and higher biocompatibility of the required materials. The temperature rise with these MNPs occurs if exposed to an external alternating current magnetic field (AMF) [38-45]. Further, the advances in chemistry also helped to target the MNPs at cancer cells, making MHT a truly localized treatment. MHT has certain advantages over other modalities like a) the AMF is generally harmless to the tissues (up to 4.85×10^8 $Am^{-1}s^{-1}$), b) the AMF can regulate the MNPs sitting deep inside without making direct contact, c) MNPs can be utilized for repeated treatments and d) heating ability can be improved by modifying the properties of MNPs. The properties of MNPs can be altered by suitable doping or changing their size and shape [46-56].

Figure 1.1: Magnetic Hyperthermia equipment (Magnetherm, nanoTherics, U.K.)

1.2.1 Mechanism of induction heating

Magnetic materials are classified as diamagnetic, paramagnetic, ferrimagnetic, ferromagnetic and antiferromagnetic materials. Out of these, ferromagnetic and ferrimagnetic with higher saturation magnetization ($M_S > 20$ Am^2/kg) values are found to be suitable for MHT application [3, 10, 25, 57, 58]. However, it is a prime requirement to have sufficient biocompatibility for the materials as the target for applications are humans. Hence, in place of ferromagnetic metals or alloys (e.g. Fe, Co, or Ni-based), the ferrimagnetic iron oxides (*viz.* Fe_3O_4 or γ-Fe_2O_3 based) are preferred due to the suitable compatibility of later ones [59-65]. Further, below a critical size the ferro or ferrimagnetic become superparamagnetic (SPM) as their coercivity (H_C) and remanence (M_r) values become zero [2, 10, 19, 66].
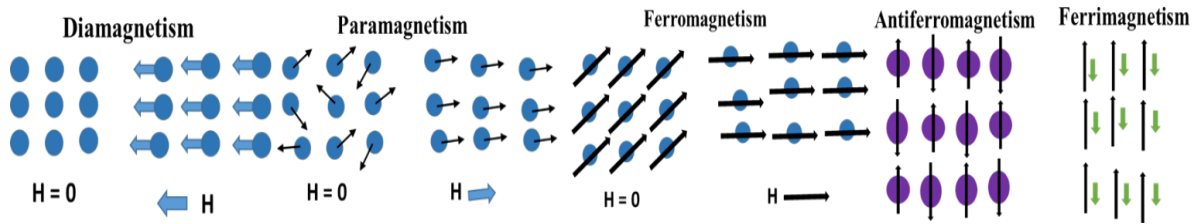
Figure 1.2: Schematic representation of magnetism of materials.

Further, due to microscopic size of biological entities (e. g. cell, 10–100 μm, virus, 20–450 nm, protein, 5–50 nm, or gene, 2 nm wide and 10–100 nm long), the required magnetic materials need to be in the nanoscale [4, 9, 17, 19, 67]. Hence, the MNPs of particle size below 30 nm are reported to be more suitable for MHT applications [68-73]. Nevertheless, these materials have a significantly high surface to volume ratio and a natural tendency for aggregation [74-76]. Therefore, the modification of their surface is essential to prevent aggregation and simultaneously enhance their biocompatibility. Such modifications facilitate the homogenous dispersion of these MNPs in carrier fluids, which is popularly known as ferrofluid [31, 36, 38]. Such ferrofluids are easy to inject inside the body intravenously. The organic materials like dextran, citric acid, chitosan, starch, PEG, PVA, pluronic acid, oleic acid and inorganic ones such as SiO_2, carbon etc. are the common materials used for this purpose [6, 8, 26, 77].
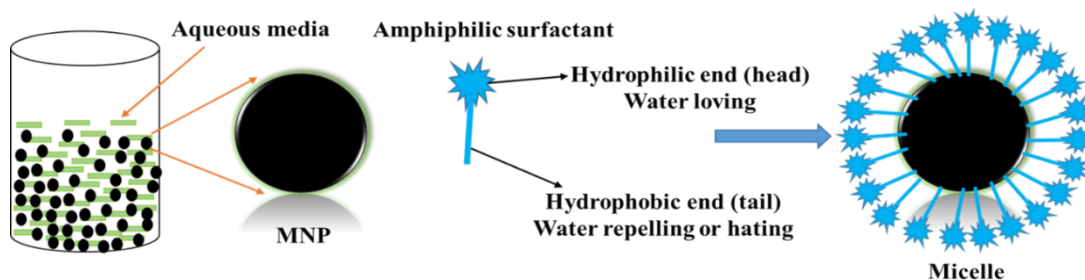

Figure 1.3: Representation of surfactant interactions with MNPs for colloidal stability.

4

The heat generation by magnetic materials, when exposed to the AMF, depends on the following losses:

a) Hysteresis loss: Magnetic materials show hysteresis loop when subjected to an external magnetic field whose amplitude is varied from zero to a maximum value and then the field is decremented to zero and scanned to a maximum negative value. The width of the loop is larger for hard magnets than for soft magnetic materials. However, no such loops are observed for SPM having an extremely smaller size (5-20 nm). Thus, the exposure of magnetic materials to AMF generates heat due to hysteresis loss. However, such loss is relatively low for softer magnets. In contrast, the SPM do not exhibit hysteresis loss.

b) Néel relaxation: In this case, particle is stationary, but the magnetic moment inside it rotates along the crystalline axes when external field is applied to change its magnetic orientation. Thus, this relaxation is due to the thermally driven continuous fluctuations of the magnetic moments. It is generally observed for nanometric sized monodomain particles and in SPM. For such particles, the thermal energy ($k_B T$) is sufficient to overcome the anisotropy energy barrier that separates opposite orientation states of the magnetic moments. Under an external AMF, heat dissipation is a function of Néel relaxation time (τ_N) which is the lag between the orientation of the magnetic moment of the nanoparticle as it crosses the energy barrier between easy magnetic axes and the direction of the applied field. Its value ranges between 10^{-9} to 10^{-10} seconds. The Néel relaxation time for a magnetic material can be given as [78, 79]:

$$\tau_N = \tau_o \, e(KV/k_B T) \quad\quad\quad\quad\quad 1.1$$

where τ_o is the attempt time or time during which the magnetic moment has sufficient energy to cross the anisotropic barrier between magnetization states ($\sim 10^{-9}$ s), K, the anisotropy constant for the material of volume V at temperature T(K), and k_B is the Boltzmann's constant.

However, the optimum heat dissipation will be obtained when the frequency of the applied external field is equal to the τ_N i.e. at a frequency above 1 MHz, but such a frequency is prohibited for the clinical applications.

c) Brownian relaxation: For this case, the MNP_S are assumed to be rotating physically, and the magnetic moment stays along the direction of crystalline axes. Therefore, heat dissipation occurs due to shear stress or frictional losses between the surfaces of MNP_S and its carrier fluid. However, this relaxation mainly depends on the hydrodynamic properties, specific heat capacity of the carrier fluid, viscosity etc. It can be expressed as [78, 79]:

$$\tau_B = 3\eta V_h/k_B T \ldots\ldots\ldots\ldots\ldots\ldots\ldots\ldots\ldots\ldots\ldots.1.2$$

where η is the viscosity of the carrier liquid, V_h is the hydrodynamic volume of the particles, k_B, Boltzmann's constant, and T is the absolute temperature.
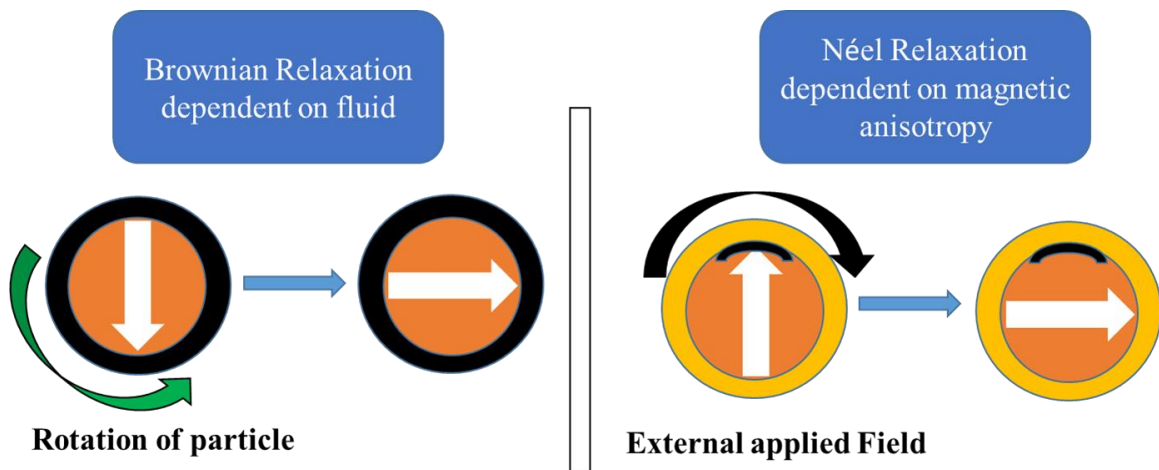

Figure 1.4: Schematic of the Brownian and Neel Relaxation loss.

Due to the higher resistivity values of magnetic iron oxides, eddy currents losses do not contribute to heating during MHT. Thus for monodomain MNPs, only the relaxation mechanisms (Néel and Brownian) provide heating. Further, it is essential to define a parameter to compare the induction heating performance of different materials when exposed to the external AC magnetic field. The term for this is known as specific power loss (SLP), which provides the heating ability of magnetic nanoparticles in the presence of external AMF$_S$. The SLP are estimated as follows [1, 28, 80]:

$$SLP\ (W/g) = C_w*(V_S/m)*(dT\ /dt)_i \ldots\ldots\ldots\ldots\ldots\ldots\ldots 1.3$$

where C_w is the specific heat capacity of water 4.2 $Jg^{-1}K^{-1}$, V_S is the volume of the suspension or ferrofluid, m is the mass of MNP$_S$, and $(dT/dt)_i$ is the initial heating rate (T *vs.* t plot) considered from 30 to 36 °C using the linear fitting technique. During the calculations for SLP values, it only considers the properties of the MNP$_S$ and carrier liquids. Nevertheless, the temperature rise during MHT also depends on the amplitude and frequency of the external AC field. Therefore, Intrinsic Loss Power (ILP) values are estimated for a better comparison of the heating abilities of various MNPs at different AMF$_S$. The ILP (nHm^2kg^{-1}) values for the ferrofluids at different fields are estimated by following equation [1, 3, 8, 80]:

$$ILP = \frac{SLP}{H^2 f} \quad \ldots\ldots\ldots\ldots\ldots..\ldots\ldots\ldots\ldots\ldots\ldots\ldots 1.4$$

where H is the magnetic field amplitude, and f is the frequency of the AC magnetic field.

1.2.2 Reported materials used for the MHT application

For the last two decades, researchers have extensively employed both ferro/ferrimagnetic (e.g. FePt, FeCo, pure and substituted Fe_3O_4/γ-Fe_2O_3) for

bioapplications [31-38, 67, 69]. The former materials (e.g. bulk Fe, FeCo etc.) though have higher saturation magnetization (M_S ~220 Am^2/kg), but its toxic nature restricts for biological implementations [1, 3, 69, 75, 78]. However, these metallic nanoparticles can be used for biological applications after encasing inside biocompatible novel materials (e.g. Pt, Au and Ag etc.) [5, 20, 28, 35, 46, 49, 59]. However, this is not cost-effective and reduces the M_S values. Nevertheless, the magnetite/maghemite based materials show enough biocompatibility without any encapsulation and are used directly with biological entities [2, 7, 29, 37, 48, 50, 79]. But, these iron oxides (Fe_3O_4/γ-Fe_2O_3) have lower M_S (e.g. ~88 Am^2/kg) values as compared to that of bulk iron [1, 5, 25, 39, 71]. As stated earlier, researchers have utilized pure or substituted iron oxide based MNPs (γ-$M_xFe_{2-x}O_3$ and $M_xFe_{3-x}O_4$) for this application [3, 9, 16, 29, 36, 45].

In contrast, several forms of iron carbides such as Fe_3C, Fe_5C_2, Fe_7C_3, $Fe_{2.2}C$ etc. are reported in the literature [31, 35, 37, 49]. Out of these carbides, Fe_3C (cementite/cohenite) has technological importance due to its characteristics. This intermetallic compound has a stoichiometric composition of 6.67 % carbon and 93.3 % iron (Fe) by weight [31, 37, 38, 40, 45]. It has an orthorhombic crystal structure, a high melting point (1837 °C), non-pyrophoric and strong magnetic (M_S, for bulk ~ 130 Am^2/kg) behavior [5, 31, 38, 74]. It is normally classified as a ceramic due to its high hardness and brittleness. Apart from that, it is expected to have superior biocompatibility than the bulk iron. Thus, the required amount of MNP_S to attain therapeutic temperature range (42-46 °C) during MHT may be smaller than iron oxide because of its higher M_S value [1, 4, 18, 22, 62]. Moreover, it is remarked that the magnetic iron oxide (e.g. Fe_3O_4 based) MNP_S gets oxidized in some of the carrier fluids with time. Further, the Curie

temperature (T_C) values for Fe_3O_4 and γ- Fe_2O_3 are 585 and 645 °C, respectively, whereas, Fe_3C has 210 °C [2,7, 10, 18, 74, 80]. Thus, the T_C values can be reduced near therapeutic temperature either by decreasing the particle size or by suitable substitutions [2, 7, 15, 19, 40]. More important, there is barely any literature on the biocompatible study of Fe_3C or its substituted nanoparticles.

1.3 Photocatalysis

The global energy crisis and the environmental pollution generated while solving it is a significant challenge for the present world [82-86]. Many researchers are putting efforts for the environment protection and to develop new clean energy sources [87-90]. In this context, the purification of chemical industries wastewater and its dissociation into H_2 molecule using solar energy is a potential field for research [91-94]. Needless to say that H_2 is a clean fuel and has a considerable potential to meet the current global energy demands due to its high-energy capacity, environmental benignancy [82, 87, 89, 95]. The conventional methods applied for dye remediation from wastewater are often expensive, inefficient, and produce secondary waste products [88, 94, 96]. However, for pollutant elimination and solar energy conversion, the semiconductor photocatalysts in UV and visible range (200-700 nm) are seen as possible materials [84, 87, 90, 97].

1.3.1 Principle of semiconductor photocatalytic process

The word photo is related to the light and catalysis refers to a matter participate in the chemical process, which increases the rate of a reaction by reducing the activation

energy without being altered till the end and without involving itself [82, 94, 97, 98]. The semiconductor photocatalyst is irradiated with photons having energies higher than that of the semiconductor's band gap, E_g (eV). Then, an electron is transferred to the conduction band and leaving behind a positive hole in the valence band [99-102]. The pair of photo excited charges that occur within a particle is called an electron-hole pair (EHP), which acts as a photocatalytic substrate by producing highly reactive radicals that can oxidize organic compounds. The energy required by a photon to generate an EHP in a photocatalyst can be related to its wavelength [86, 103-109].

$$\lambda \, (nm) \leq 1240/E_g\ldots\ldots\ldots\ldots\ldots\ldots\ldots\ldots\ldots\ldots\ldots\ldots\ldots\ldots..1.5$$

Whereas, the efficiency of a photocatalyst is measured in terms of the number of reactions occurring per photon absorbed. It depends on the rate of the generation, the fate of migration, and energy levels of the photo excited EHPs, their band gap, size, and surface area [84, 88, 110]. The fates of the EHPs determine the reactions that occur within the particle and on its surface [111]. The schematic diagram represents the possible reaction pathways for the semiconductor photocatalytic process is shown in Fig. 1.5.
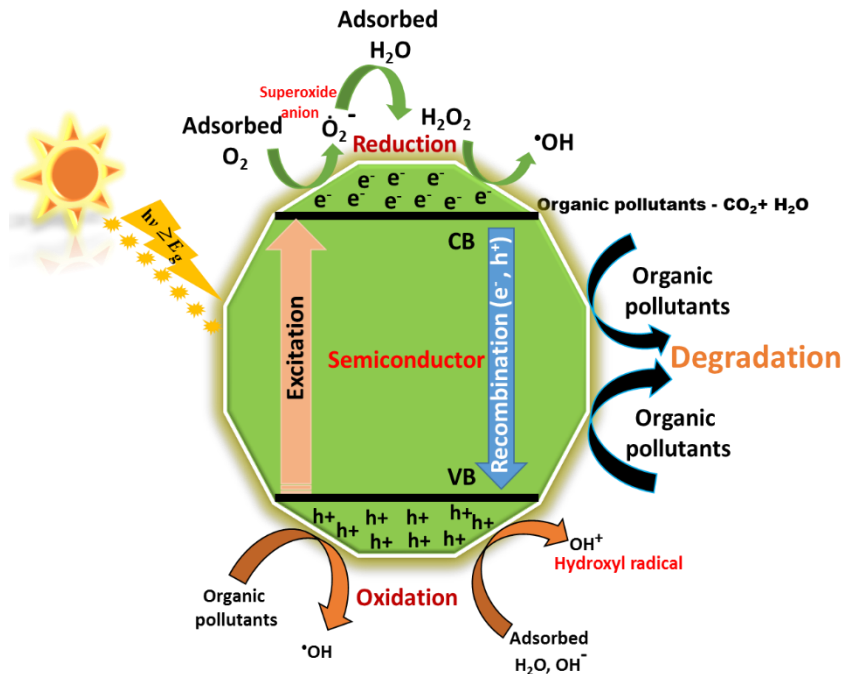
Figure 1.5: Schematic diagram shows the reaction mechanisms during the semiconductor photocatalytic process.

1.3.2 Importance of electron and hole pairs (EHPs)

For the high-performance semiconductor, charges (electrons/holes) must be freely migrated to the surface of the particle and interact with adsorbed species [86, 88, 112]. The photogenerated electrons that can migrate to the surface are primarily used in the reduction of O_2 (liquid/gas solutions), and other reactive species such as the superoxide radical O_2^- or the singlet oxygen, which can stimulate other radical chain reactions involving H_2O_2 or O_3 as shown in Fig. 1.5 [89, 93, 98, 113]. The photogenerated holes migrate to the surface and oxidize organic species with lower oxidation potentials or create the highly reactive and short-lived hydroxyl radical $^•OH$ upon the catalyst's adsorption of H_2O [83, 90, 98, 114].

11

1.3.3 Factors affecting photocatalytic performance

The photocatalytic efficiency depends on the percentage of EHP$_S$ interacting with the adsorbent species, but only less than 10% participated in the reaction. The rest EHP$_S$ recombines either in volume or on the surface leading to lower efficiency of photocatalysis. The time taken for the EHP recombination is either in a picosecond or nanosecond, which depends on the following factors [104, 115]:

➢ Dye concentration
➢ Catalysis amount
➢ pH value
➢ Size and structure of the photocatalyst
➢ Surface area of the particles
➢ Reaction temperature
➢ Concentration and nature of pollutants
➢ Effect of light intensity and irradiation time
➢ Dissolved oxygen
➢ Effect of dopants on dye degradation

1.3.4 Materials utilized for photocatalysis application

TiO_2 is utilized as a primary material for photocatalysis due to its better photoactivity, lower cost, photochemical stability, biocompatibility, and environmental-friendly features [82, 87, 105]. However, its wider band gap (~3.2 eV) limits efficacy due to the rapid recombination of photogenerated electron-hole pairs. Nevertheless, numerous efforts have been waged to enhance its efficiency either by numerous dopings or forming composites such as N-doped Fe–TiO_2, $CaIn_2O_4$/Fe-TiO_2, Prussian blue/TiO_2, Fe-Sn-TiO_2, Sn-doped TiO_2 and CuO coupled Sn–TiO_2, etc. [107, 109, 116-119].

In the recent past, investigators utilized visible-light-driven (VLD) magnetically separable photocatalysts made up of γ-Fe_2O_3@SnO_2, Fe_3O_4@TiO_2@Ag, Fe_3O_4@TiO_2,

bean-like core/shell $Fe_3O_4@C@Cu_2O_{35}$, α-$Fe_2O_3@TiO_2$ and α-$Fe_2O_3/Ag/SnO_2$ etc. [88, 118, 120-124]. Amongst these, Fe_3O_4 nanoparticles enthralled more because of its decent magnetization, electrical resistivity, optical (narrow band gap) properties and low toxicity [103, 108, 123]. The magnetite acts as a carrier, which enhances the recycling efficacy and can be collected after the reaction using a permanent magnet [89, 99, 101]. Nevertheless, this material also displays a high recombination rate of the photogenerated electron-hole pairs. Moreover, these shortcomings are resolved either by forming a core-shell structure or by improving the visible light absorption [87, 89, 91, 125]. The shells on Fe_3O_4 are usually made from carbon-based materials (activated carbon, carbon nanotubes and graphene) or ceramics (e.g. SiO_2 and Al_2O_3) that prevent its chemical dissolution and the entrapment of electrons by the magnetic core [126]. Further, the incorporation of noble metals (e.g. Ag) improves its visible light absorption efficiency. On the other hand, the carbonaceous materials having a porous structure, suitable electronic properties and adsorptive capacity further enhance the applicability of Fe_3O_4 [98, 113, 127]. Photocatalytic activity found to be enhancing even after doping of transition metal ions (e.g. Ni, Cu, Fe, Cr, etc.) or reactive nonmetal ions (e.g. C, N, S, F, etc.) [128]. These donor/acceptor ions promote either transfer or separation of electrons/holes and thus enhance the performance. Amongst these, Ni-ion has higher potential as it generates optimum hydroxyl radicals in the visible region [87, 95, 114, 127]. The radicals further reduce the recombination of the photo-generated electron-holes and improve photo-conversion efficiency. Moreover, at a lower concentration, Ni-ions capture electrons and create a p-n junction to improve the charge separation.

Nevertheless, after an optimal concentration, the space charge region becomes narrow, which intensifies photogenerated electron-hole pair recombination [84, 108, 128].

Though there are literatures on photocatalytic applications of transition metal oxides with carbon based materials but such studies are lacking for Fe_3C materials. Iron carbide has lower Fermi level and higher conductivity due to its metallic nature. Further, its low cost and higher magnetization value make it a relatively suitable candidate. In addition, carbon protects Fe_3C from chemical oxidation and simultaneously promotes the transfer of photogenerated electrons which improves the photocatalytic performance [31, 37, 38]. However, its composites either with Fe_3O_4 or with C, may change the conductivity significantly.

1.4 Electrochemical energy storage devices (LIB$_S$)

Recent studies advocate on the great necessity to develop renewable energy technologies to meet the ever-growing global energy demand and to cope up with the rapid depletion of fossil fuels [129-133]. Hence, the use of clean and renewable energies based on solar cells, fuel cells, supercapacitors, and metal-ion based batteries have become emerging research fields [130, 134]. Amongst the alternative energy sources, electrochemical energy storage devices have attracted significant consideration due to their higher efficiency and lesser pollutant generation [132, 135-137].

Further, the consistent escalating energy demands for portable electronic devices and hybrid electric vehicles have stimulated research and development of Li-ion batteries (LIBs) [138]. These high-performance batteries have large power density and excellent cycling stability [131]. The commercially available LIBs generally consist of layered rock salt-type $LiCoO_2$ as the cathode material, graphitic carbon as the anode material,

and non-aqueous organic solvents containing Li salts as the electrolyte solution [129, 139]. The three components modulate the performance of these batteries. The metal-based batteries in general and LIBs in particular are employed as the power source for small portable electronic gadgets, electric vehicles as well as hybrid electric vehicles [136, 140].

1.4.1 Construction and Principle of LIB

The basic construction of the cells is very similar regardless of its chemistry. It consists of four main parts: anode, cathode, separator, and electrolyte [136]. The goal of the battery is to create electron flow, which creates current and can be used to power up LEDs, bulbs, electronics, motors, etc [133, 138]. The cathode and anode are made up of two dissimilar materials and separated by an electrolyte that can accommodate charged species [139]. One is more comfortable to give up electrons while the other is more willing to accept them. The separator ensures the anode and cathodes do not touch (short) and allows lithium ions to flow through. The electrolyte used as a medium of oxidation/reduction process and ions to flow between the anode and cathode. In the discharge mode, when the battery serves to drive the electric current, an oxidation process takes place at the negative electrode (anode), resulting in electrons moving from the electrode through the circuit [137, 140-141]. Lithium ions simultaneously flow from the anode to the cathode through the electrolyte material. A complementary reduction process takes place at the positive electrode (cathode), replenished by electrons from the circuit. The cell voltage largely depends on the potential difference of the electrodes, and the overall process is spontaneous [137]. The schematic diagram of the Li-ion battery is shown in Fig. 1.6.
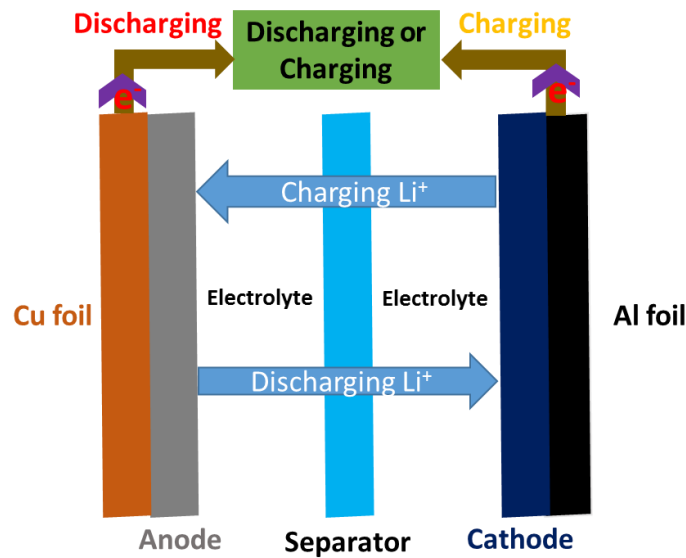
Figure 1.6: Schematic representation of Li-ion battery.

1.4.2 Desirable characteristics for electrode materials

   a) <u>For anode:</u>

➢ Significant capability of Li-ion adsorption

➢ Excellent cyclability

➢ Low reactivity against electrolyte

➢ Fast reaction rate

➢ Low cost

➢ Environment-friendly and non-toxic

   b) <u>For cathode:</u>

➢ High discharge voltage

➢ High energy capacity

➢ Long cycle life

➢ High power density

➢ Light weight

➢ Low self-discharge ability

➢ Pollutants free

1.4.3   Materials utilized as anode for LIB$_S$

For all the LIB$_S$ applications, graphite is usually implemented as anode due to its low cost, high stability, good cyclability, and suitable electronic conductivity [129, 131, 140]. However, the lower specific capacity (372 mAhg^{-1}), reduced rate capability and possibilities of intercalation of smaller Li$^+$ ions between the graphite layers limit its wider acceptance [141-143]. Thus, there is an utmost necessity to develop safer and high-capacity anode materials that can substitute graphite. For this purpose, researchers replaced graphitic anode by transition metal oxides (e.g. Fe$_3$O$_4$), which displayed two and half times more theoretical specific capacity (928 mAhg^{-1}) [142-144]. In addition, the oxides are inexpensive, biodegradable, non-toxic and have relatively easy synthesis routes [47, 144]. Nevertheless, such oxides suffer from low electrical conductivity, high initial capacity loss, significant volume change and poor durability, thus impeding their applicability [145-147]. Moreover, the formation/decomposition of thick solid electrolyte interphase (SEI) due to the movement of Li-ions reduces their capacity and may lead to battery failure [148].

Nevertheless, a carbon encapsulation over the anodes (e.g. Fe$_3$O$_4$ or Fe$_3$C or both) creates adequate internal voids space, which mobilizes Li-ions and hence improves the electronic conductivity as well as the performance [149-153]. On the other hand, the transition metal carbides (TMC) are found to be more stable as they undergo the least volume change and exhibit longer cycles. Moreover, the TMCs have metallic structures where smaller carbon atoms get distributed in their interstitial voids [141, 154]. In contrast to metal oxides, the TMCs exhibit higher electronic conductivity, mechanical

stability and corrosion resistance. Simultaneously, they diminish the volume change of the parent electrode materials during cycling.

Therefore, researchers have explored various nanocomposites of iron oxides and iron carbides for this purpose. For example, Tour et al. fabricated Fe_2O_3/Fe_3C–graphene thin films with three-dimensional nanopores *via* a low-temperature CVD method, Guo et al. synthesized robust $Fe_3O_4@Fe_3C$ yolk-shell nanospindles through pyrolysis and Zhou et al. synthesized a core-shell structured $Fe@Fe_3C/C$ composite using FeOOH rods as templates etc. The reported optimum irreversible capacity for $Fe_3O_4@Fe_3C@C$ composite anode is 1150 $mAhg^{-1}$. Such a yolk/shell structure of Fe_3C nanomaterials with sufficient internal void space acted as highly efficient anode material with high rate and long term capacities. Recently, it is also reported in the literature that iron carbide (Fe_3C) has sound catalytic activity and improves the electrochemical performance of the yolk-shell shaped $Fe_3O_4@Fe_3C@C$ anodes. Further, Fe_3C played a crucial role as a catalyst to preserve the structural integrity of Fe_3O_4 from dissolution with electrolyte after the number of cycles due to its high thermal stability, high resistance against oxidation and excellent mechanical strength. The Fe_3C/C nanocomposite has shown a stable discharge capacity of 750 $mAhg^{-1}$ after 120 cycles at 1000 mAg^{-1}, which is more significant than pure carbon electrodes. Additionally, the reduction in the SEI component and improvement in the reversible capacities was also observed due to Fe_3C. Therefore, scientists are exploring new materials based on Fe_3C.

1.5 Synthesis of the nanocomposite materials

There are a few reports on the synthesis of Fe_3C nanoparticles. However, to synthesize this material, $Fe(CO)_5$ used as a precursor, which is not readily available and synthesis yields byproducts such as carbides/nitrides/oxides of iron or even pure Fe along with this carbide.

Table 1.1: Synthesis protocols, phases and saturation magnetization (M_S) values.

Sr. no	Synthesis Route	Precursors	Phases	M_S (emu/g)	References
1	Sol-gel	Gelatin, $FeCl_3$, chitosan	Fe_3C	110	Cristina Giordano et al./Chem. Mater.
2	Laser pyrolysis	$Fe(CO)_5$	$Fe_{2.2}C/Fe_5C_2$	202	Marc Respaud et al./ Nano Lett.
3	Biopolymer route	Alginic acid, iron acetate	Fe_3C/Fe_3O_4	60	M. Sharma et al./ J. Magn. Magn. Matr.
4	Sol-gel	$FeCl_3$, melamine	Fe_3C/Fe	106	Wang, X., et al./ J. Mater Sci: Mater Electron
5	Sol-gel	$FeCl_3$, Urea	Fe_3C/Fe	86	X. Wang et al. / J. Magn. Magn. Matr.
6	Sol-gel	$FeCl_3$, $Ni(CH_3CO_2)_2$ $\cdot 4\, H_2O$	Fe_3C	30	X. Wang et al. /J. Alloys Compd.
7	Sol-gel	$FeCl_3$, HMTA	Fe_3C	30	P. Zhang et al. /Mater Res Bull
8	Solvothermal	$FeCl_3$, HMTA, EDA	Fe_3C	80	X. Wang et al./ Dyes and pigments
9	Microwave refluxing	$FeCl_3$, $FeSO_4.7H_2O$	Fe_3O_4	60	M. Srivastava et al./J. Alloys Compd.

The conventional techniques utilized for fabrication of this carbide include as flame spray pyrolysis, Fischer-Tropsch, laser ablation method, sol-gel, solvo-thermal, and by direct carburization at high temperature. Similarly, for the synthesis of the Fe_3O_4, numerous methods

are available in the literature, such as the co-precipitation method, wet chemical method, microwave refluxing, hydrothermal, solvo-thermal, and polyol etc. The routes opted for the synthesis will also affect the structural properties. However, in this present dissertation, the urea assisted sol-gel technique was utilized for the preparation of nanocomposite of Fe_3C or substituted (Zn, Ni, and Mn) Fe_3C/Fe_3O_4 with carbon. The synthesis process is discussed in detail in the experimental part (Chapter-2).

1.6 Structural and magnetic properties

1.6.1 Iron carbide (Fe₃C)

Several forms of iron carbides such as Fe_3C, Fe_5C_2, Fe_7C_3, $Fe_{2.2}C$ etc. are reported in the literature [17, 21, 28]. Out of these carbides, the present dissertation focused only on Fe_3C (cementite/cohenite) because of its great technological importance. It is an intermetallic compound and has a stoichiometric composition of 6.67 % carbon and 93.3 % iron (Fe) by weight. It has an orthorhombic crystal structure (carbon atoms occupy the interstices between close-packed iron atoms), high melting point (1837 °C), and non-pyrophoric [128, 141]. The orthorhombic iron carbide consists of four carbon and twelve iron atoms in a unit cell [114]. The space group of the orthorhombic Fe_3C is Pnma 62 and has Wyckoff positions of *8d* and *4c*. The lattice parameters for the bulk Fe_3C are reported as 5.089, 6.743 and 4.523, and unit cell volume 155.23Å^3 [71, 119, 147, 148]. The unit cell of the Fe_3C is drawn with the help of VESTA software and shown in Fig. 1.7. It shows that the Fe atom has two atomic sites in the orthorhombic unit cell. In addition, the stability of the Fe_3C phase is quite high, even at a high temperature ~1227 °C [71]. It is usually classified as a ceramic due to its high hardness and brittleness. It is

frequently found as an essential constituent in ferrous metallurgy (in most steels and cast irons). The use of iron carbide during the production of steels and cast irons is remarkably environmentally friendly because of its lowest C emission as compared to that of other virgin iron steelmaking processes [71]. Also, iron carbide is much more effective and less costly than any other means to produce high-quality steel.
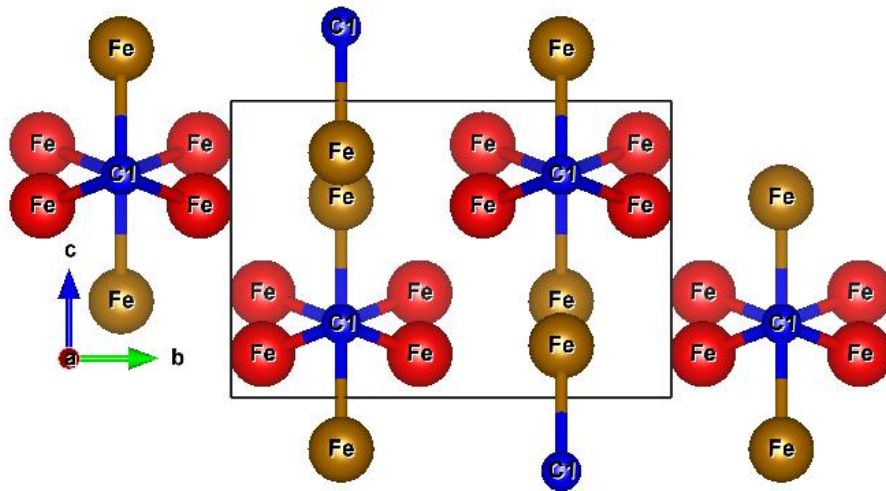

Figure 1.7: Positions of the atoms (Fe and C) of iron carbide having orthorhombic system.

1.6.2 Magnetite (Fe$_3$O$_4$)

Magnetite (Fe$_3$O$_4$) is a face-centered cubic inverse spinel crystal structure with space group is Fd-3m [118]. The chemical composition of magnetite is Fe^{2+}Fe$_2$$^{3+}O_4$$^{2-}$. The structure is inverse spinel, with O^{2-} ions forming a face-centered cubic lattice and iron cations occupying interstitial sites. Half of the Fe^{3+} cations occupy tetrahedral sites while the other half, along with Fe^{2+} cations, occupy octahedral sites [25]. The unit cell consists of 32 O^{2-} ions. The lattice parameter for the bulk Fe$_3$O$_4$ reported as 8.39 Å and unit cell

volume 590.58 $Å^3$. The polyhedral model for cubic inverse spinel structure of Fe_3O_4 was created by VESTA software which is shown in Fig. 1.8.
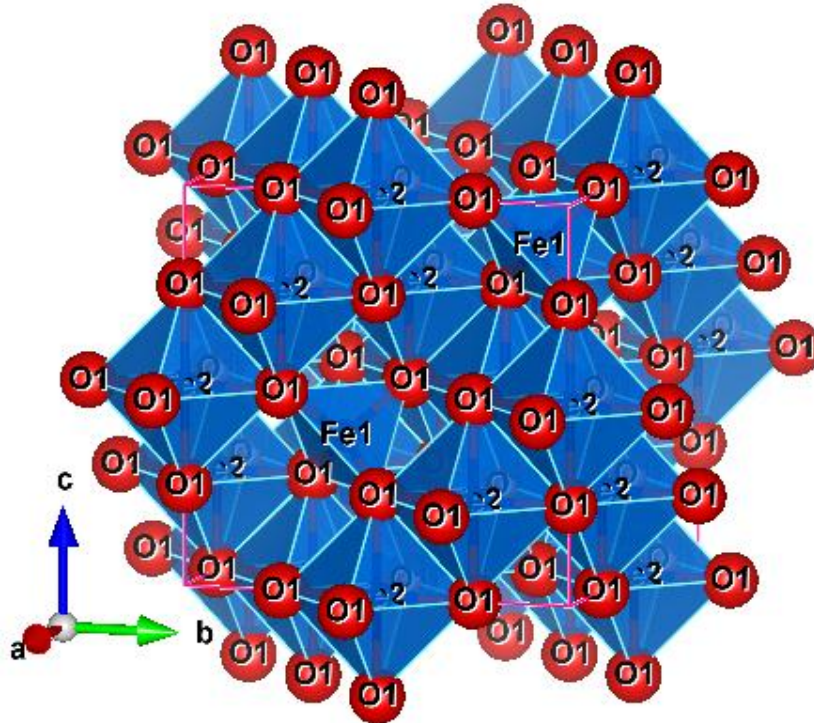

Figure 1.8: Schematic polyhedral model for cubic inverse spinel structure of Fe_3O_4.

1.7 Scope of the present investigation

As discussed earlier, Fe_3C has higher M_S values than Fe_3O_4. Further, the presence of carbon makes more biocompatible, which is desirable for the MHT and photocatalysis as well as for anode materials.

The present study deals with the synthesis of ferromagnetic Fe_3C or substituted (Zn, Ni, and Mn) Fe_3C/Fe_3O_4 nanocomposite with carbon for the above applications. The sol-gel technique followed by calcination, is utilized for the synthesis of these composites. It is clear from the literature that, small fraction of the substitution can alter their

microstructure as well as their magnetic properties. For MHT application, the suitable magnetic properties of the substituted iron carbide or oxide can be modulated by doping of atoms or cations respectively. These atoms or cations either reduce or enhance the M_S values due to the formation of the antiferro or ferromagnetic coupling respectively. In the present thesis, Zn, Ni and Mn are substituted in Fe_3C and Fe_3O_4. These all are formed antiferromagnetic coupling with Fe atoms, which results in a reduction in the M_S values.

The present doctoral thesis includes the structural, morphological, and magnetic studies of the nanocomposites as mentioned earlier. Further, the heating performance (adiabatically) of these MNP_S based aqueous ferrofluids were examined at various field and frequencies. It is observed that these aqueous ferrofluids have enough potential to attain the therapeutic temperature (42-46 ℃) for killing the cancerous cell. The cytotoxicity assessments of their ferrofluid were carried out by Sulforhodamine B assay (SRB) with human lung adenocarcinoma A549 cells. So far, our knowledge is concerned, there is no report on in-vitro study with these materials in the literature.

Recently, investigators have utilized visible-light-driven (VLD) magnetically separable photocatalysts made up of γ-Fe_2O_3@SnO_2, Fe_3O_4@TiO_2@Ag, Fe_3O_4@TiO_2, bean-like core/shell Fe_3O_4@C@Cu_2O_{35}, α-Fe_2O_3@TiO_2 and α-Fe_2O_3/Ag/SnO_2 etc. Fe_3O_4 nanoparticles interested much because of its magnetization, electrical resistivity, optical (narrow band gap) properties and low toxicity. The magnetite acts as a carrier which enhances the recycling efficacy and can be recollected using a magnet. On the other hand, the carbonaceous materials (e.g. graphitic C, graphene etc.) having a porous structure, suitable electronic properties and adsorptive capacity which further enhance the applicability of Fe_3O_4/C nanocomposites. Photocatalytic activity found to be

enhanced even after doping of transition metal ions (e.g. Ni, Cu, Fe, Cr, etc.) and reactive nonmetal ions (e.g. C, N, S, F, etc.). These donor/acceptor ions promote either transfer or separation of electrons/holes and thus enhance the performance. Amongst these, Ni-ion has higher potential as it generates optimum hydroxyl radicals in the visible region.

This iron carbide has a lower Fermi level and higher conductivity due to its metallic nature. Further, its low cost and higher magnetization value make it a relatively suitable candidate. Also, carbon protects Fe_3C from chemical oxidation and simultaneously promotes the transfer of photogenerated electrons which improves the photocatalytic performance. However, its composite either with Fe_3O_4 or with C, will change its conductivity. As stated, Ni has a significant influence on electron-hole recombination. It prompted us to prepare nanocomposites of Fe_3C/C, $Fe_3C/Fe_3O_4/C$ and $Ni-Fe_3C/Fe_3O_4/C$ for photocatalytic application. The structural and morphological as well as photocatalytic properties of these nanocomposites were carried out using photo-Fenton degradation of the p-nitrophenol (PNP) and methyl orange (MO) pollutant dyes.

Furthermore, this present study deals with the electrochemical energy storage devices that have attracted significant consideration due to their higher efficiency. The escalating energy demands for portable electronic devices and hybrid electric vehicles have inspired the researchers to look for high-performance Li-ion batteries (LIBs) which display high power density and excellent cycling stability. Initially, graphite is usually implemented as an anode, but its lower specific capacity (372 $mAhg^{-1}$) limits applicability. For this purpose, researchers replaced graphitic anode by transition metal oxides (e.g. Fe_3O_4), which displayed two and half times more theoretical specific capacity (928 $mAhg^{-1}$) but high initial capacity loss, significant volume change and poor

24

durability impede their applicability. To overcome these limitations carbon encapsulation over the anode (e.g. Fe_3O_4 or Fe_3C or both) creates adequate internal voids space which improves the performance of the anode material. On the other hand, the transition metal carbides (TMC) are found to be more stable as they undergo the least volume change and exhibit longer cycles.

Finding continuous improvement in the discharge capacity for Fe_3O_4, Fe_3C or their composites with or without C inspired us to carry out the work presented in the thesis. Hence, we synthesized Fe_3C/C and Mn-substituted (Fe_3C and Fe_3O_4)/C nanocomposites by a simple and inexpensive sol-gel method. The purpose of Mn substitution in the Fe_3C/Fe_3O_4 was to observe the effect. Thus, in order to find out the electrochemical performance of these nanocomposites, Voltammograms profiles, Galvanostatic lithiation/delithiation profiles, and coulombic efficiencies were studied extensively.